

1 **Vertical structure of chlorophyll-a during marine heatwaves in the**
2 **California Current Ecosystem**

3 **Jian Li^{1,2,3}, Arthur J. Miller², Qi Wang⁴, Dillon J. Amaya⁵, Peiliang Li^{1,3,6}, Yanzhen Gu^{1,3,6*},**
4 **Peng Bai^{7*}**

5 ¹Ocean College, Zhejiang University, Zhoushan, China

6 ²Scripps Institution of Oceanography, University of California, San Diego, La Jolla, USA

7 ³Hainan Institute, Zhejiang University, Sanya, China

8 ⁴Marine Academy of Zhejiang Province, Hangzhou, China

9 ⁵NOAA/Physical Sciences Laboratory, Boulder, USA

10 ⁶Hainan Observation and Research Station of Ecological Environment and Fishery Resource
11 in Yazhou Bay, Sanya, China

12 ⁷Marine Science and Technology College, Zhejiang Ocean University, Zhoushan, China

13

14 **Corresponding author*:**

15 Yanzhen Gu (guyanzhen@zju.edu.cn), Peng Bai (pengbai@zjou.edu.cn).

16

17

18

Abstract

In the past decades, the California Current Ecosystem has experienced intense marine heatwaves, which have induced significant disruptions to local phytoplankton communities. Here, using 30-year cruise observations, we identify a previously undocumented vertical structure in chlorophyll-a concentration response to marine heatwaves, characterized by reductions in the surface layer coupled with increases in the subsurface. By integrating observations and coupled physical-biogeochemical model products, we demonstrate that declines of surface chlorophyll-a are primarily attributed to suppressed nutrient upwelled to the upper ocean. Although surface irradiance increased modestly (+3.5%), light availability in the subsurface layer improved substantially (+21.7%) due to reduced phytoplankton shading at the surface. Concurrent with enhanced lateral nutrient transport, phytoplankton growth at depth was promoted during heatwave events. This study highlights the pivotal role of subsurface phytoplankton dynamics in shaping the vertical chlorophyll-a concentration structure and its variability under extreme events.

Introduction

Marine heatwaves (MHWs), defined as prolonged episodes of anomalously warm seawater temperature^{1,2}, have shown increasing frequency and intensity over the past century and are projected to intensify further under global climate change^{3,4}. Accumulating evidence demonstrates that these extreme events exert cascading impacts on marine ecosystems, including mass coral bleaching⁵, critical habitat degradation⁶, ecosystem regime shifts⁷ and unprecedented biodiversity loss⁸. Moreover, MHWs are increasingly being examined along with concurrently occurring biogeochemical extremes⁹, such as acidity and hypoxia^{10,11,12}, which can exacerbate the responses of sensitive marine organisms^{12,13}. Such ecological disruptions fundamentally compromise the provision of essential ecosystem services¹⁴. Given their escalating frequency, unpredictable spatiotemporal patterns, and potentially irreversible ecological consequences, MHWs have emerged as a pressing global concern^{14,15,16}.

As the foundation of marine primary production, phytoplankton regulate key biogeochemical processes including carbon sequestration, nutrient cycling, and food web dynamics^{17,18}. Their biomass and community structures can be significantly influenced by MHWs due to their various sensitivities to thermal anomalies, with cascading effects on productivity and functional diversity^{19,20}. Previous studies demonstrated that MHWs exert spatially heterogeneous impacts on phytoplankton across regions and events^{21,22}. Generally, surface chlorophyll-a concentration (CHL) decreases in the tropics and mid-latitudes while it increases at high latitudes during MHWs²³, with these patterns governed by alterations in nutrient dynamics^{21,24,25}, light availability²², and iron limitation²⁶. Concurrently, phytoplankton community structures tend to exhibit a universal shift toward smaller species during MHWs, altering energy transfer efficiency through marine food webs^{24,27,28,29}.

The California Current Ecosystem (CCE), where CalCOFI (The California Cooperative Oceanic Fisheries Investigations; Fig. 1) is located, experienced multiple severe MHWs

in recent decades, driven by synergistic atmospheric-oceanic forcing mechanisms including intensified North Pacific High variations^{30, 31}, reduced coastal upwelling³², and anomalous poleward current transport³³. Therefore, a growing body of research has documented MHW-induced impacts on phytoplankton within CCE. For example, during the 2014–2015 MHW, often called “the Blob”, suppressed upwelling and intensified stratification reduced the nutrient supply to the euphotic zone, causing significant declines in phytoplankton biomass and net primary production in CCE³⁴. Meanwhile, to adapt to the abnormal temperature and nutrient conditions, phytoplankton community shifted toward smaller cells^{27, 35, 36}, and harmful algal bloom events in nearshore were also related to MHWs^{37, 38}.

Increasing evidence indicates that MHWs are not confined to the surface layer but may extend to deeper waters^{9, 39}, with potentially increased duration and intensity in some cases^{40, 41}. Therefore, vertically propagating extremes represent an emerging topic in recent MHW research^{11, 13}. These studies revealed that the subsurface compound events (MHW, low oxygen and high acidity) are often associated with vertical displacements of water masses, have shown significantly intensification in recent decades¹³, and are projected to be enhanced under global warming¹¹. However, the vertical response of phytoplankton communities to MHWs remains relatively understudied due to limited data availability^{42, 43}. Recent findings by⁴³ have highlighted a pronounced decoupling between surface and subsurface phytoplankton biomass during the past decade of ocean warming in the Sargasso Sea. That study underscores the limitations of remote sensing observations and emphasizes the critical role of vertical structures in examining biogeochemical responses to extreme events.

Such vertical decoupling raises critical questions about the underlying mechanisms and whether they differ during short-term extreme events like MHWs compared to gradual, long-term ocean warming. In predominantly nutrient-limited systems like the CCE, the vertical structure of CHL exerts a more critical influence on marine biogeochemical cycling and carbon export potential than surface CHL alone⁴⁴. However, our current

understanding of MHW impacts on CHL remains disproportionately focused on epipelagic phytoplankton responses, leaving critical knowledge gaps regarding vertical heterogeneity in phytoplankton dynamics during extreme warming events, thereby hindering our ability to predict ecosystem resilience and climate feedback mechanisms.

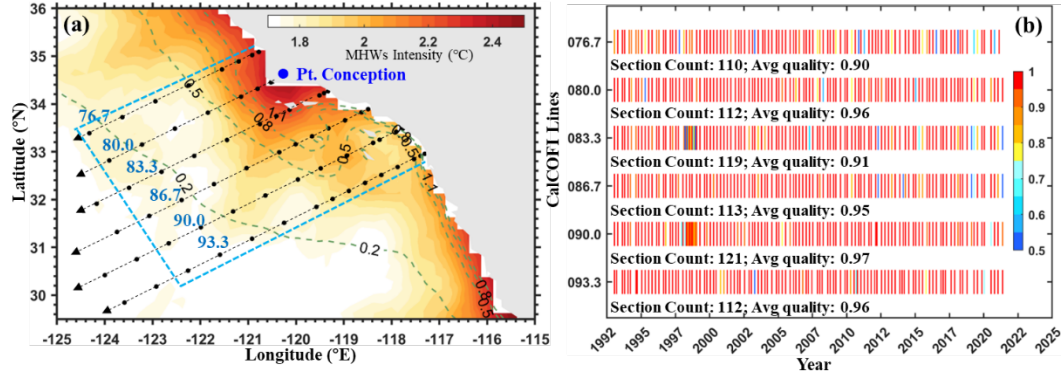


Fig. 1 MHWs in the CCE and data records of the CalCOFI. (a) Mean MHW intensity based on OISST from 1993 to 2022. Black dots and dashes represent the sampling stations and transect lines of CalCOFI cruises. Green dashes represent the mean surface CHL concentration from Copernicus-GlobColour (1997–2022). Blue box denotes the boundary of the CalCOFI region. (b) Sampling records and its data quality (proportion of valid data) of six CalCOFI Lines from 1993 to 2022.

In this study, we observed a previously undocumented phenomenon in the CalCOFI region that the vertical response of CHL to MHWs is not uniform, but exhibits a distinct vertical structure characterized by negative surface anomalies overlying positive subsurface anomalies (Herein, we define the “surface” as extending from the sea surface to the subsurface chlorophyll maximum layer (SCML) depth, and the “subsurface” as the water column beneath the SCML depth). Using in situ observations from CalCOFI, we systematically characterize the vertical CHL anomaly structure and associated environmental conditions during MHWs. We further employ physical (PHY) and biogeochemical (BGC) model outputs from the Copernicus Marine Environment Monitoring Service (CMEMS) to investigate the underlying mechanisms driving this vertical pattern. This study aims to advance our understanding of the vertical response of phytoplankton to MHWs and provide valuable insights into their ecological consequences in upwelling systems.

Results

MHWs in CCE region

In the past 30 years (1993–2022), intense MHWs were predominantly concentrated along the coastal CCE region that contains the highest phytoplankton biomass (Fig. 1a), particularly around Point Conception, where the averaged MHWs intensity exceeds 2.3 °C. Correspondingly, this region experiences severe declines in surface CHL (Supplementary Fig. 1-2). To characterize the temporal evolution of these events, we further examined the monthly mean MHWs intensity and spatial coverage of the study area (blue box in Fig. 1a), as a function of time. The results (Fig. 2a) indicate that the most severe and frequent events occurred during positive Pacific Decadal Oscillation (PDO) years (Fig. 2b), which are typically associated with suppressed coastal upwelling and increased net downward surface heat flux⁴⁵. Here, a given month is labeled as “MHW month” if more than 50% of the study area experiences MHW condition and the regional mean intensity exceeds 1 °C. Based on this definition, a total of 68 MHW months were identified between 1993 and 2022. Among these, 23 CalCOFI cruises (* in Fig. 2) were conducted under MHWs in CCE, providing valuable in situ observations to assess ecosystem responses to extreme warming.

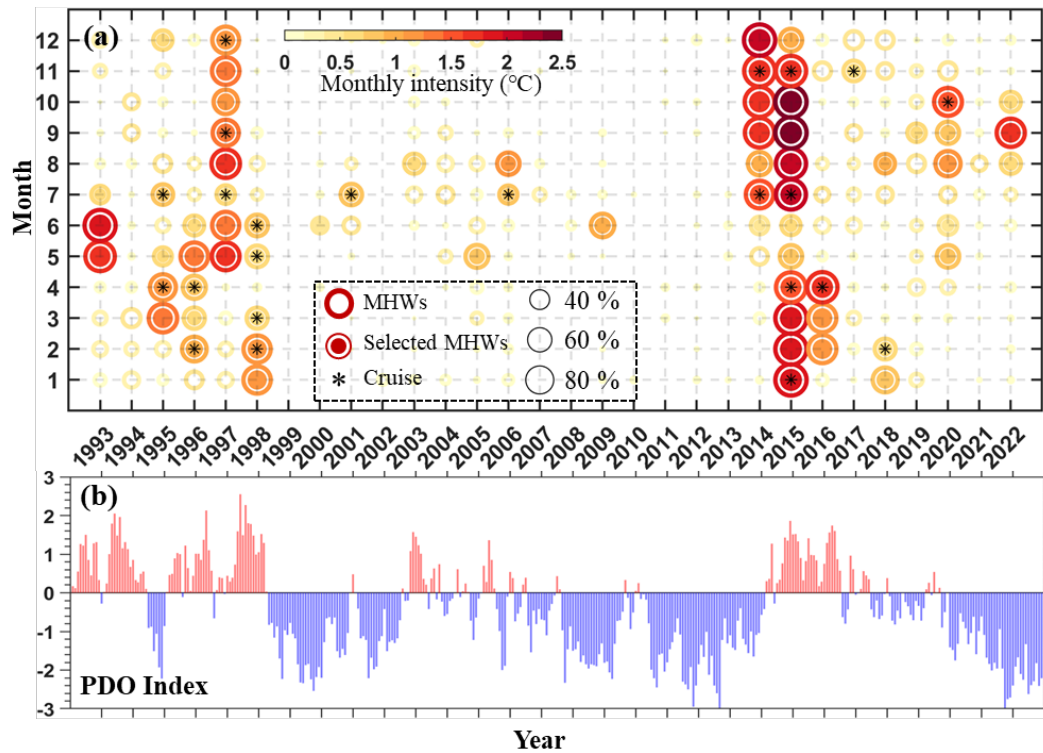


Fig. 2 MHWs occurrences and PDO index. (a) MHW occurrences in the CalCOFI region based on OISST. Color and radius of unfilled circles represent the monthly mean intensity and spatial coverage (%) of MHWs, respectively. Filled circles indicate months when more than 50% area (Fig. 1) is under MHW conditions and the regional mean intensity exceeds 1 °C, labeled as “MHW month”. Asterisks denote MHW months when CalCOFI cruises were conducted. (b) Pacific Decadal Oscillation (PDO) Index.

Vertical CHL responds to MHWs

Based on 687 sections derived from 6 CalCOFI cruise lines collected between 1993 and 2022, we computed CHL anomalies ($N = 35754$) within the 200-m depth water column during MHWs (filled circles with asterisks in Fig. 2) to examine the vertical response of CHL to these extreme events (Fig. 3a). Intriguingly, we observed an unexpected vertical structure in the CHL pattern, characterized by negative anomalies in the surface layer accompanied by positive anomalies at depth, which has rarely been captured in this region by previous studies relying on satellite observations or vertically integrated investigations. In order to better quantify this phenomenon, we further assessed the vertical distribution of CHL anomalies at each depth level within the CalCOFI region (Fig. 3b). The results reveal a significantly reduction in CHL (mean: $0.08\text{--}0.15\ \mu\text{g L}^{-1}$)

from surface to 50 m depth, with a concurrent increase ($0.01\text{--}0.05\ \mu\text{g L}^{-1}$) below 70 m depth during MHWs. The maximum negative anomalies occur at depths of 20–40 m, while the most pronounced positive anomalies were located around 70–80 m depth. Although the magnitude of subsurface positive anomalies was much smaller at individual depths compared to surface negative anomalies, their cumulative effect remains substantial when vertically integrated ($-2.85\ \mu\text{g L}^{-1}$ at surface versus $1.62\ \mu\text{g L}^{-1}$ at subsurface, exceeding 50% of the surface reduction magnitude), presenting a non-negligible contribution when estimating variability of vertically integrated CHL. This vertical redistribution may help explain why no significant correlations were previously found between MHW intensity/duration and vertically integrated CHL⁴⁶, despite surface CHL showing strong statistically significant correlations with MHWs. It may also elucidate the unexpected positive depth-integrated CHL anomaly during 2015–2016 El Niño in the CCS⁴⁷.

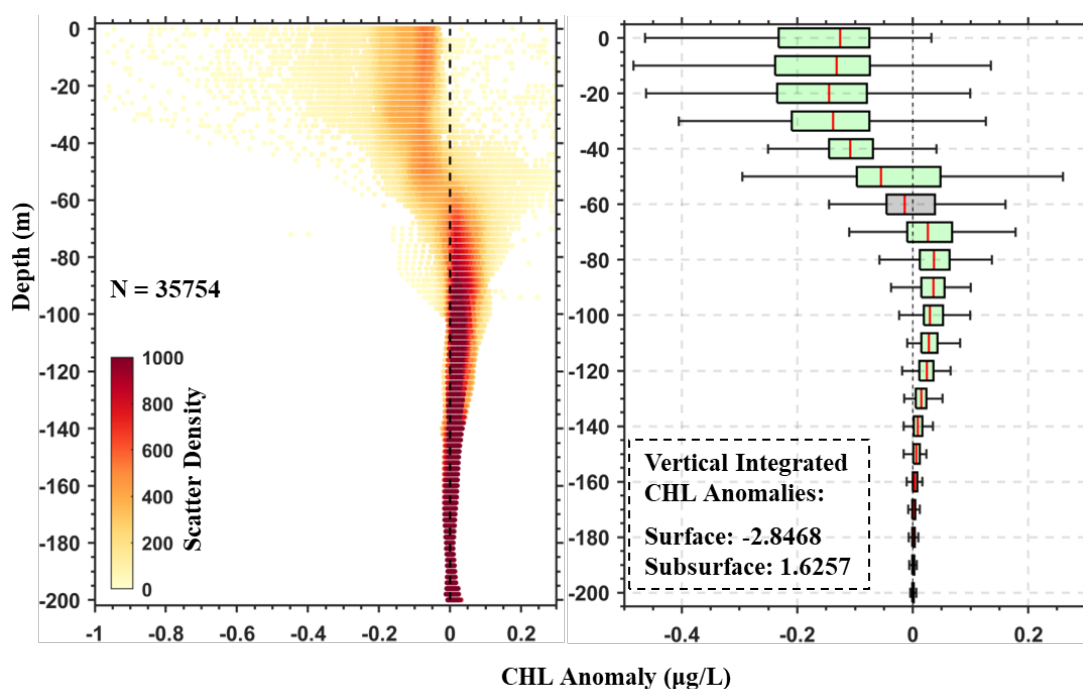


Fig. 3 Vertical responses of CHL to MHWs. (a) Scatter density plot of CHL anomalies during MHWs, derived from vertical profiles at all stations across six CalCOFI lines. (b) Boxplot of CHL anomalies at 10-m depth intervals. The vertical dashed line indicates zero anomaly, and red lines denote the median. Green boxes indicate depths where anomalies are statistically different from zero (T-test; $p < 0.05$). Vertically integrated CHL anomalies were calculated separately for the surface layer (from surface to SCML depth) and the subsurface layer

(SCML depth to 200-m) at each station, and then averaged across all stations within the CalCOFI region.

Since this phenomenon was consistently observed across all CalCOFI transects, we selected Line 90.0 for detailed analysis due to its relatively higher sampling density and superior data quality (Fig. 1b; described in the Data and Methods) to better understand the vertical structure of the CHL anomalies. Composite anomalies of all variables shown in Fig. 4 and Fig. 5 were averaged over MHW months during which CalCOFI cruises were conducted (asterisks in Fig. 2).

Composite temperature anomalies across four seasons show that the most intense warming events happened during winter and fall⁴¹. Previous studies have demonstrated that vertical advection, which is associated with wind-driven reduced upwelling^{9, 29, 39, 41, 48, 49, 50} and deepened thermocline³², constitutes the dominant driver of MHW development in the CCE. Thus, warming signals are observed in the subsurface across all four seasons, with particularly intensified warming at depth during winter due to weak stratification^{40, 41}. Fig. 4e-h illustrate the seasonal distributions of CHL anomalies along Line 90.0, offering insight into phytoplankton responses to MHWs. This vertically decoupled variability was detected across all seasons, extending from onshore to offshore regions. The maximum reduction in CHL occurs around the SCML depth (red dashed lines in Fig. 4e-h), whereas CHL exhibited anomalous increases below the SCML during warming events. Due to the varying nutrient and physical environments between onshore and offshore, the SCML does not occur at a fixed depth but deepens as the offshore distance increases. Consequently, layers around 60-m depth (gray bar in Fig. 3b) contain positive anomalies onshore but negative anomalies offshore, resulting in no statistically significant change during MHWs when anomalies are depth-aggregated.

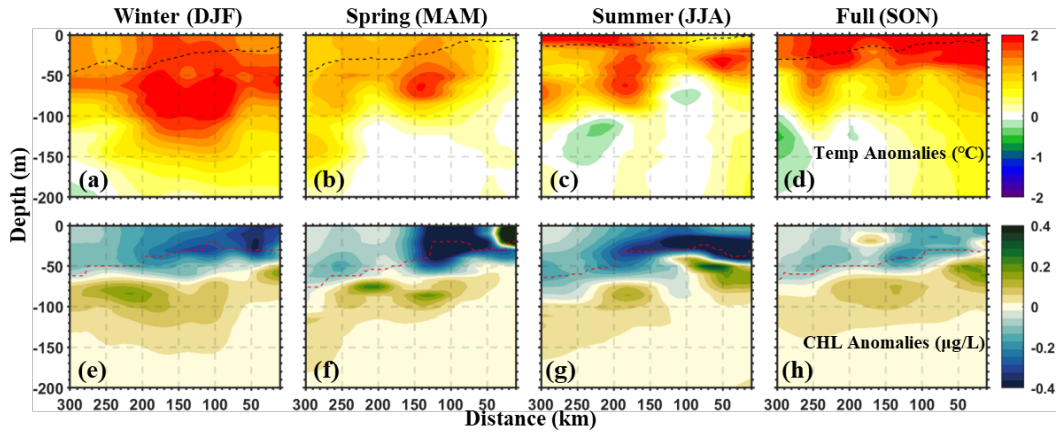


Fig. 4 Seasonal patterns of vertical CHL and temperature anomalies. Seasonal anomalies of temperature (a-d) and CHL (e-h) during MHWs along CalCOFI Line 90.0 (DJF, MAM, JJA, SON represent winter: December–February, spring: March–May, summer: June–August, and fall: September–November, respectively). Black and red dashed lines denote mixed layer and subsurface chlorophyll maximum layer (SCML) depth, respectively. Anomalies were calculated based on data from MHW months during which CalCOFI cruises were conducted (asterisks in Fig. 2).

This finding highlights a decoupled vertical structure in CCE phytoplankton dynamics during MHWs, whereby subsurface phytoplankton biomass anomalies contradict the conventional paradigm of the reduced CHL pattern. The significant negative anomalies of surface CHL, which have been widely reported in the CCE, were mainly driven by reduced nutrient availability due to weakened upwelling^{29, 36, 51}. However, the subsurface positive anomalies have rarely been documented, and the underlying mechanism remains unclear, challenging our understanding of MHW-induced ecological disturbances in the CCE. Therefore, the remainder of this study focuses on elucidating the mechanisms governing subsurface CHL enhancement during MHWs in this eastern boundary upwelling system.

Environmental Anomalies During MHWs

Vertical variability in CHL is regulated by both hydrodynamic and biogeochemical processes⁴⁴. Thus, we examined the variability of key environmental variables during MHWs along CalCOFI Line 90.0 (Fig. 5a-h) to explore the potential drivers of subsurface CHL anomalies. Composite temperature anomalies reveal that the most

intense warming occurs 100–200 km offshore, extending from the surface to the ~100 m depth. In addition, salinity significantly increased in the upper 100 m layer, possibly due to the enhanced evaporation from warmer seawater or to weakened transport of fresher waters from the north. Below 100 m depth, salinity shows a negative anomaly at a similar distance (100–200 km from the coast), and its distribution indicates that the negative salinity anomaly originates from deeper layers. According to the abovementioned mechanism of the MHWs in this region as well as the distribution of warming signal, these salinity anomalies indicate a reduction in the upward transport of salt deep water—consistent with suppressed upwelling. Additionally, negative salinity anomalies near the offshore boundary of the transect imply that lateral intrusions may also contribute to the observed freshening, as projections under future warming scenarios have indicated⁵².

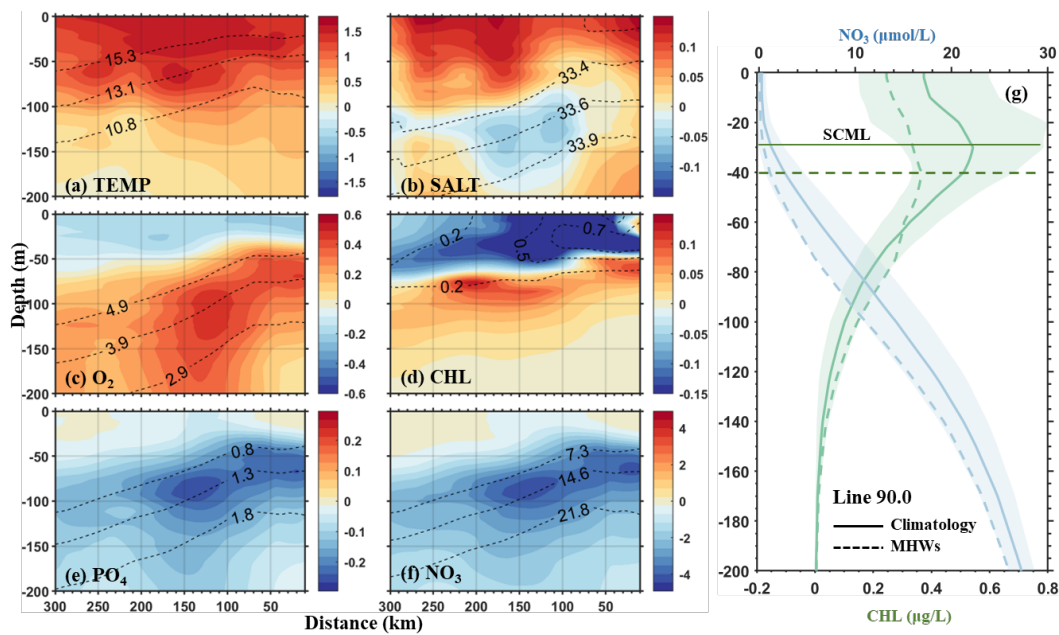


Fig. 5 Composite anomalies of environmental variables during MHWs. (a–f) Composite anomalies of temperature (TEMP; °C), salinity (SALT; PSU), dissolved oxygen (O₂; ml L⁻¹), CHL (μg L⁻¹), phosphate (PO₄; μmol L⁻¹) and nitrate (NO₃; μmol L⁻¹) during MHWs, with contours representing climatological values. (g) Vertical profiles of CHL (green), SCML (dark green) and nitrate concentration (blue) under climatology (solid lines) and MHWs (dash lines) states, averaged along offshore distance of CalCOFI Line 90.0.

For the nutrient environment, as expected, phosphate and nitrate show consistent

declining patterns along their respective isolines throughout the water column during MHWs, with the strongest reductions occurring between 50 and 100 m depth, coinciding with the depths of maximum CHL positive anomalies. Along the cross-shore direction, nutrient depletion was most pronounced between 100 and 200 km from the coast, where suppressed upwelling occurred. These nutrient patterns likely reflect a combined effect of weakened upwelling and enhanced consumption by increased subsurface phytoplankton biomass. Positive oxygen anomalies exhibited a similar subsurface pattern with the nutrients, further supporting the interpretation that observed nutrient reductions are driven by both physical and biogeochemical processes. Notably, other biogeochemical processes, such as the remineralization and grazing, may also contributed to the patterns of CHL, oxygen and nutrients during MHWs. However, in this study, we mainly focus on the possible variations driven by the growth and mortality of the phytoplankton.

Overall, compared with climatological conditions, the SCML deepened by approximately 8 m (Fig. 5i), and the average nitracline depth (defined as the depth where nitrate concentration first exceeds $1 \mu\text{mol L}^{-1}$) also deepened from 21 to 33 m depth during MHWs. Such shifts are consistent with prior findings in this region^{46, 51}. Moreover, this decoupled pattern becomes more pronounced as MHW intensity increases (Supplementary Fig. 3), with the magnitude of the subsurface anomalies increasing accordingly.

To further support our descriptions of local physical and biogeochemical variability, we incorporated output from CMEMS BGC and PHY numerical models. Prior to utilizing BGC-derived variables, we conducted comprehensive validation against satellite and in-situ observations (see Supplementary Note. 1). In general, the model demonstrates satisfactory performance in simulating CHL dynamics within the study region (Supplementary Fig. 4-5) and, critically, it successfully reproduces the vertically decoupled CHL structure and associated nutrient-oxygen patterns observed during MHWs (Supplementary Fig. 6), showing good agreement with the CalCOFI data (Fig.

5). Outputs from the PHY model were not further validated, as its skill has been well established in this region^{31, 53, 54}.

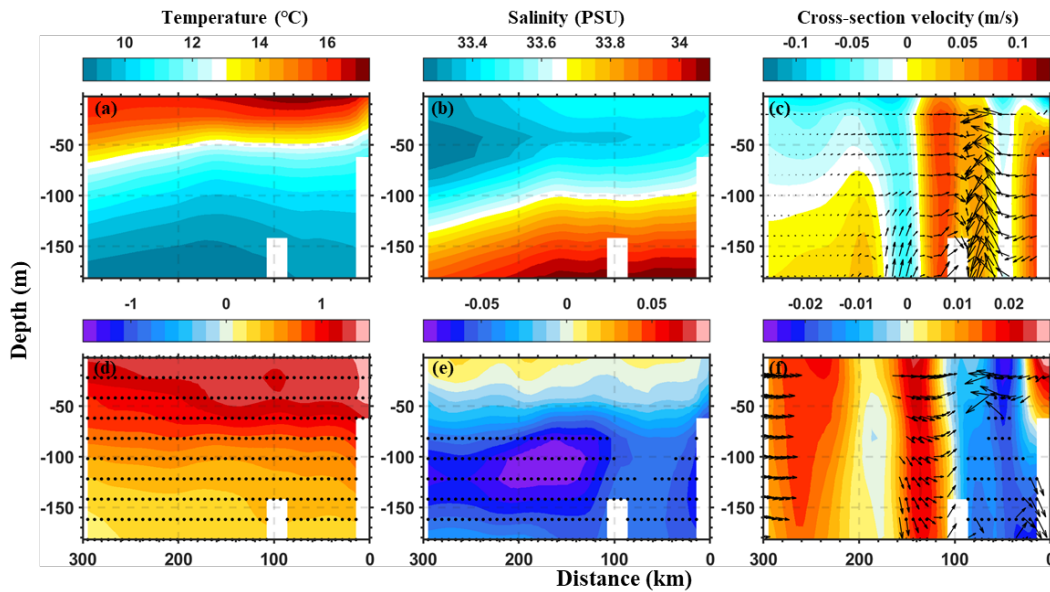


Fig. 6 Physical conditions during MHWs. Climatological (a-c) profiles of temperature, salinity and cross section velocity and their composite anomalies (d-f) during MHWs along CalCOFI Line 90.0. Black dots denote the anomalies are significantly different from zero (T-test; $p < 0.05$). Arrows in (c) and (f) represent the mean along-section and vertical velocities and their anomalies (only shown when anomalies in both directions are significantly different from zero), vertical component of velocity is multiplied by 1000 for better visualization. Note that the composite anomalies are calculated by the same MHW month as Fig. 5.

Vertical profiles of simulated physical variables clearly reproduce the key dynamic processes described above (Fig. 6). Maximum salinity anomalies occurring 100–200 km offshore below 100 m depth exhibit clearer extension both towards the depth and further offshore (Fig. 6e). A significant upwelling zone indeed exists within this offshore band, with its intensity significantly reduced during MHWs (Fig. 6f). Additionally, enhanced eastward advection was also observed offshore, potentially transporting fresher waters toward the upwelling region. Notably, anomalies in Fig. 6 were computed as the deviations from monthly climatology (whereas those in Fig. 5 are based on seasonal climatology derived from observations).

Discussion

The subsurface environmental conditions described above explain the mechanisms driving the observed positive CHL anomalies. While the composite patterns in nutrients and oxygen anomalies likely result from weakened upwelling combined with enhanced phytoplankton activity, they do not directly account for the positive anomalies in subsurface phytoplankton biomass. To better understand the drivers of enhanced subsurface CHL during MHWs, it is necessary to further investigate the event-scale dynamics shaping this response. We therefore focused on the representative 2014–2015 MHW in the CCE to investigate the key mechanisms underlying this vertical structure.

Unlike the large-scale North Pacific warming event (“the Blob”), the 2014–2015 MHW along the California Coast are primarily driven by intermittent air-sea heat flux, horizontal and vertical heat advection anomalies^{33,55}. Specifically, MHW in 2014 was driven by both anomalous vertical heat advection and air-sea heat flux⁵⁵, whereas in 2015, alongshore heat advection (increased poleward volume transport and warmer-than-average temperature of the California Undercurrent) also contributed to the anomalous warming, in addition to the aforementioned drivers³³. In addition, both years featured notable positive cross-shore heat advection anomalies³³. With the primary physical drivers of the 2014–2015 MHW established, we next investigate the vertical CHL dynamics and associated environmental parameters within the CalCOFI region (Fig. 7). Anomalies are calculated as deviations from monthly climatology (averaged over the CalCOFI region), with long-term signals (more than 5 years) removed using a high-pass Butterworth filter.

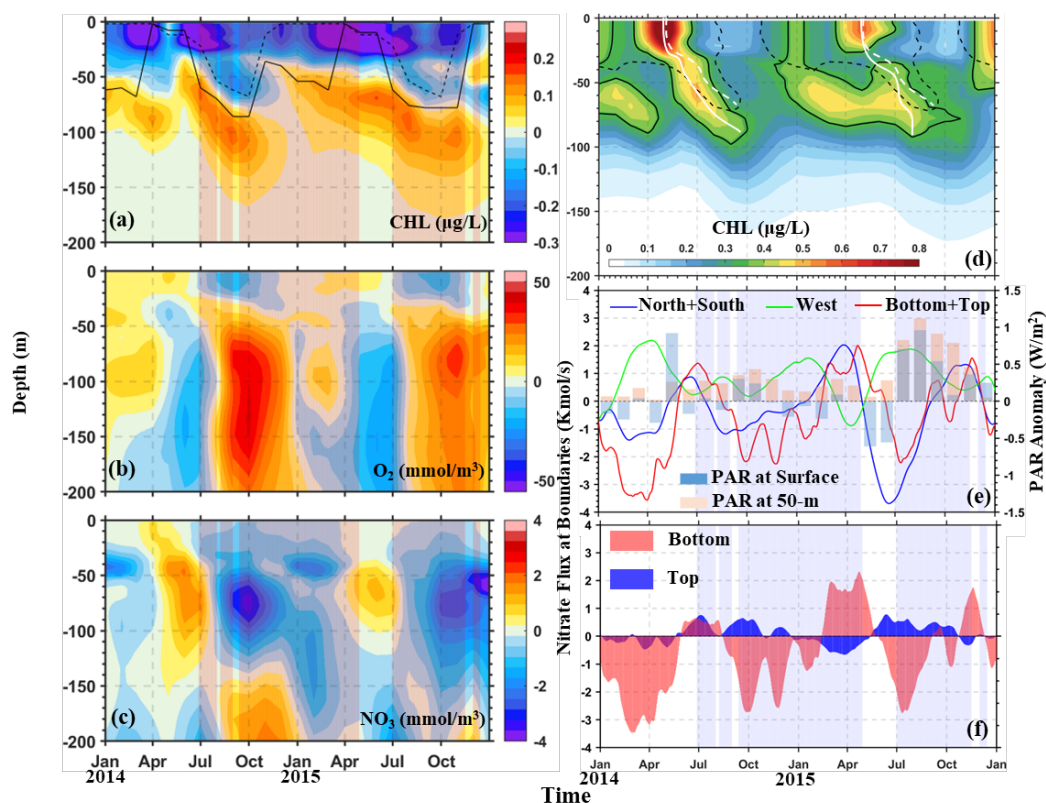


Fig. 7 Temporal evolutions of local biogeochemical environments and nitrate flux. (a-c) Vertical anomalies of simulated CHL, dissolved oxygen and nitrate, averaged over the CalCOFI region, shown as a function of time. Dashed and solid lines in (a) refer the climatological and real SCML depth, respectively. (d) Modeled vertical CHL distribution from 2014 to 2015. Dashed and solid contours (white lines) represent the climatological and real $0.4 \mu\text{g L}^{-1}$ CHL isoline (SCML), respectively. PAR at surface is divided by 5 for visualization. (e) Nitrate flux anomalies across the five boundaries of the CalCOFI region: alongshore (blue), cross-shore (green), and vertical (red), with positive values indicating inward transport. Blue and red bars denote anomalies of PAR at the surface and 50-m depth, respectively. (f) Nitrate flux anomalies across bottom and top boundaries.

Model simulations revealed that positive subsurface CHL anomalies initially occurred around 50 m depth and progressively deepened to ~ 150 m as the MHW developed (Fig. 7a). More specifically, the seasonal chlorophyll bloom that typically originates in April 2014 and persists through August in climatology, was suppressed before July due to MHW disruption (solid and dashed black contours in Fig. 7d). Concurrently, phytoplankton exhibited deeper and more pronounced subsurface growth (solid and dashed white lines in Fig. 7d), contributing to the positive anomaly. This anomaly attenuated with the seasonal shoaling of the SCML around November (black lines in

Fig. 8a). During a subsequent proliferation phase in January 2015 (Supplementary Fig. 7), surface productivity was again suppressed under stronger MHW conditions (Supplementary Fig. 8), with enhanced growth occurring below 50 m depth.

Our analysis of environmental variable anomalies in the CCE, integrated with established theoretical frameworks of phytoplankton dynamics^{24, 36, 44, 51, 56}, suggests that nutrient dynamics is a primary driver governing vertical CHL variability. However, the phytoplankton biomass would be expected to decline rather than show positive anomalies as the SCML deepens due to reduced nutrient availability in deep waters⁵⁷. In such cases, light availability may become another dominant factor, especially when phytoplankton grow below the climatological euphotic depth. In highly productive coastal system like CCE, underwater light conditions depend not only on surface irradiance but also on vertical light penetration, which is strongly influenced by water turbidity and the phytoplankton self-shading effect^{58, 59}. Thus, we quantified the Photosynthetically Active Radiation (PAR), and nitrate flux across the five boundaries of the CalCOFI region (Fig. 7f) to further assess the contributions of light availability and nutrient supply to the subsurface CHL during MHWs. Surface PAR data were obtained from the MODIS PAR product, while subsurface PAR was calculated using the same three-waveband light penetration scheme as CMEMS-BGC model. Advection and diffusion are the major physical processes that control the nitrate flux in the water column. In upwelling system like the CCE, the contribution of diffusion is generally considered minor compared to advection^{60, 61}. Thus, we mainly focus on the advection term in this study.

Positive nitrate anomalies were observed between 50 and 100 m depth prior to the onset of both MHWs in June 2014 and 2015 (Fig. 7c), potentially creating a more favorable nutrient environment for phytoplankton growth here. Nitrate flux calculations revealed positive anomalies across all three spatial dimensions (cross-shore: westward; alongshore: northward + southward; vertical: upward + downward) in June 2014, and the positive vertical flux resulted from both enhanced import through the bottom

boundary and reduced export through the upper boundary. In June 2015, elevated nitrate input occurred primarily through vertical and cross-shore transport (Fig. 7f). Subsequently, nitrate anomalies for both events diminished as the MHW progressed, with vertical and alongshore nitrate flux anomalies turning negative. Positive cross-shore nitrate fluxes were observed during nearly all events between 2014 and 2015, closely aligning with net heat advection in the same direction ³³.

Regarding the light conditions, significantly positive PAR anomalies were observed at 50 m depth throughout the 2014–2015 events, while sustained surface PAR enhancement occurred during the latter event (July to December 2015). Compared to the surface, subsurface PAR showed stronger correspondence with the vertical distribution of positive CHL anomalies, which exhibited progressive deepening in response to two distinct phases of subsurface PAR enhancement (June–October 2014 and January–September 2015). These results indicate that, although the subsurface light condition can be directly influenced by the surface irradiance, phytoplankton productivity at depth is more sensitive to light availability within these specific layers, and the self-shading effect of the phytoplankton can significantly alter the light penetration throughout the water column during MHWs. While the depth of the positive CHL anomalies aligned well with the PAR anomalies at 50-m depth, light availability alone cannot fully explain the observed subsurface phytoplankton activity. For example, the positive subsurface CHL anomaly reached its maximum intensity at 60 m depth in May 2015, despite the absence of significant subsurface PAR enhancement. In this case, enhanced productivity was primarily supported by positive nitrate anomalies transported via upwelling and cross-shore advection. Specifically, when along-shore and vertical nitrate flux anomalies were negative in June and July 2015, nitrate anomalies still remained positive due to cross-shore nitrate flux supply, suggesting the non-negligible contribution of lateral nutrient supply during warming events.

These findings suggest that light condition variations induced by atmospheric processes and phytoplankton self-shading effect might influence both the depth and intensity of

subsurface phytoplankton growth during MHWs. However, vertical and cross-shore nitrate fluxes act as critical additional drivers sustaining subsurface productivity under these anomalous conditions.

Building upon the detailed examination of specific 2014–2015 MHW events in the CCE, we further investigated the background states of these potential controlling factors during all MHWs from 1993 to 2022. Mean net nitrate flux anomalies across the five boundaries during MHWs are shown in Table 1. Compared to climatological conditions, a significant net influx of nitrate was observed from the western boundary during MHWs (1.90 kmol s^{-1} ; $P < 0.01$), while no significant anomalies were found at the northern or southern boundaries. Vertically, less nitrate ($-1.02 \text{ kmol s}^{-1}$; $P < 0.01$) was upwelled into subsurface water through the bottom boundary and reduced nitrate ($-0.38 \text{ kmol s}^{-1}$; $P < 0.01$) was exported through the top boundary, reflecting to the suppressed upwelling during MHWs. These results suggest that, although vertical nutrient supply was substantially weakened, increased lateral input from the western boundary partially offsets the overall nutrient deficit. It can be anticipated that without this supplementary input, local nutrient levels and thus phytoplankton productivity, would likely have declined even further. This finding aligns with previous projections based on climate models, which suggest that climate-driven increases in nutrient-rich water transport through the western boundary could enhance productivity in the CCE under future warming scenarios⁵². Our results, derived from observed extreme warming events, support this type of local mechanism and underscore the pivotal role of lateral nutrient transport in sustaining ecosystem productivity under MHW conditions.

Moreover, light condition in the subsurface layers showed varying degrees of enhancement under MHWs (Fig. 8a), particular during 2014–2016 MHW, the average PAR increment throughout the water column exceeded 4 W m^{-2} . In order to further examine whether this light enhancement result from increased surface irradiance influenced by atmospheric processes, or reduced self-shading effect of the suppressed surface phytoplankton biomass, we examined PAR at two layers for every event. As

shown in Fig. 8b, most MHW months exhibited positive PAR anomalies at 50 m depth, with only two exceptions showing negative values. Surface PAR also increased in the majority of events. On averaged, surface PAR in the CalCOFI region increased by 3.53% ($p < 0.01$; T-test), likely due to reduced cloud cover and enhanced incoming solar radiation⁶². However, the reduction of the surface phytoplankton significantly enhanced the light penetration in the water column, causing the subsurface PAR to significantly increase by 21.7%, which provide better light availability for the phytoplankton growth at depth. Further support for this mechanism comes from the co-location of normalized CHL and PAR anomalies during MHWs. Specifically, positive CHL anomalies emerged at depths where normalized PAR anomalies reached their maximum (shaded purple area in Fig. 8b), highlighting the tight coupling between subsurface light availability and phytoplankton growth.

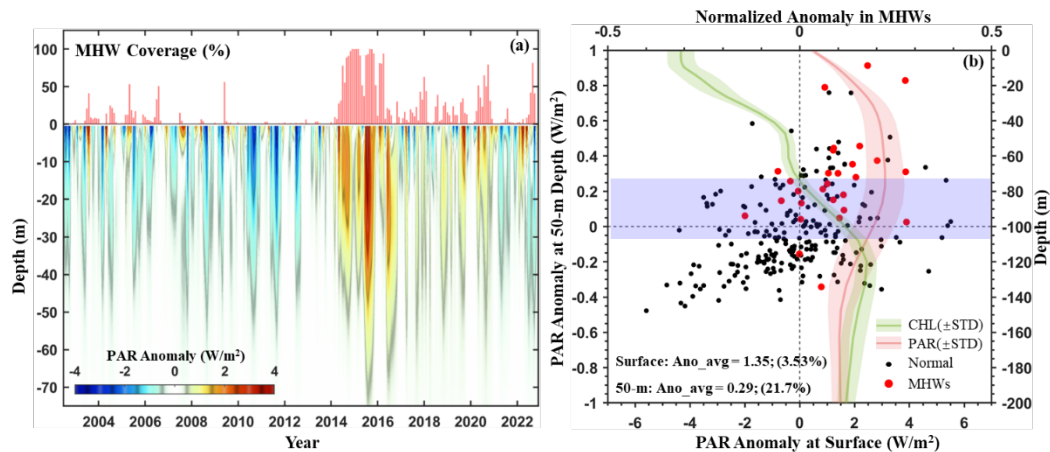


Fig. 8 Light availability during MHWs. (a) Timeseries of vertical light conditions. Red bars represent the monthly coverage of the MHW area (%). Shading denotes the PAR anomalies at different depth. (b) Black (red) dots represent the monthly PAR at surface and at 50-m depth under normal (MHW) condition. Green and red line refer normalized anomalies of CHL and PAR under MHWs. All values here are regionally averaged over the CalCOFI region.

Thus, the mechanisms underlying the vertical structure of CHL response to MHWs in the CCE become evident. Suppressed upwelling limits the nutrient delivery to surface waters, leading to a marked decline in surface CHL. Simultaneously, enhanced lateral advection of nutrient-rich waters through the western boundary provides an additional

nutrient source to the subsurface layers. Improved light penetration driven by decreased surface phytoplankton biomass, combined with increased surface irradiance, further enhance light availability in subsurface waters. The co-occurrence of lateral nutrient supply and improved light conditions promotes phytoplankton growth at depth, ultimately driving the anomalous enhancement of subsurface CHL during MHWs in the CCE.

However, despite the supplementary lateral input, composite nutrient anomalies during MHWs remain negative, suggesting that lateral nutrient import may not fully compensate for the reduced vertical supply. Additionally, under low-light conditions, the efficiency of nutrient utilization decreases⁶³, meaning that intensified phytoplankton productivity at depth consumes greater amounts of available nutrients, further exacerbating local nutrient depletion.

The vertical heterogeneity in CHL responses to climate change and extreme events has attracted increasing attention very recently. For example, in the open Arctic Ocean, diatom blooms have been observed near the seafloor rather than at the surface, owing to improved light conditions at depth⁶⁴. In the Sargasso Sea, subsurface phytoplankton biomass became increasingly decoupled from the surface community under long-term warming and enhanced stratification, leading to pronounced subsurface CHL enrichment despite surface depletion, with total phytoplankton carbon showing an overall increase over the past decade⁴³. Similarly, phytoplankton biomass in the central tropical Indian Ocean exhibits contrasting seasonal variability between surface and subsurface layers⁶⁵. Considering the projected increase in both intensity and frequency of MHWs on global scales and in CCE region^{3, 4, 66}, developing a comprehensive understanding of vertical CHL dynamic during MHWs is crucial for predicting ecosystem responses under future ocean climate scenarios.

Conclusion

In this study, we integrated long-term CalCOFI cruise observations, satellite remote

sensing data, and coupled physical-biogeochemical model products to investigate the vertical CHL response to MHWs in the CCE. Our results revealed that the vertical response of CHL to MWHs is not uniformly decreased, but exhibits vertical structure with decreases in the surface layer and increases in the subsurface layer. This pattern is inherently challenging to detect through satellite-based observations. Consistent with previous studies, the reduction in surface CHL is primarily attributed to suppressed nutrient supply due to weakened upwelling. In contrast, the increase of subsurface CHL is linked to two key processes: (i) enhanced lateral nutrient transport through the western boundary, which provide additional nutrient supply under low-level nutrient conditions caused by reduced upwelling; (ii) improved light availability at depth, resulting from both increased surface irradiance and enhanced light penetration due to reduced surface phytoplankton biomass.

To date, satellite remote sensing remains the most effective way to monitor phytoplankton dynamics in various spatial scales. However, it is inherently limited to near-surface signals and may miss significant subsurface variability, where phytoplankton communities are often more abundant and more sensitive to environmental perturbations⁴³. Our findings suggest that subsurface phytoplankton may play an important role in shaping the vertical CHL structure and its response to extreme climate events. These insights provide valuable perspectives for interpreting biogeochemical variability and assessing ecosystem responses across trophic levels under future ocean warming scenarios^{46, 67}.

Finally, we must acknowledge the limitations of this study, particularly our exclusion of biological processes such as zooplankton grazing and physiological behavior of phytoplankton, which remain difficult to observe and simulate accurately. Further, enhanced in-situ observations, such as those carried out by the CCE-LTER in process cruises⁶⁸ and systematic sensitivity experiments using advanced coupled physical-ecological models in the CCE^{69, 70, 71, 72} are necessary for comprehensive quantification of the regulatory mechanisms governing these complex vertical CHL dynamics during

487 MHWs.

488 **Data and Methods**

489 **In Situ Sampling Data**

490 In situ observations were obtained from the bottle database collected during quarterly
491 CalCOFI cruises, including 6 transect lines (93.3 to 76.7) in the CCE (Fig. 1a). Vertical
492 profiles of seawater temperature, salinity, dissolved oxygen, chlorophyll-a
493 concentration and nutrients (phosphate, nitrite) from 1993 to 2022 were analyzed. The
494 anomalies of these environmental variables during MHWs were computed as deviations
495 from seasonal climatology for each transect.

496 Although CalCOFI generally conducts four cruises per year, sampling frequency has
497 varied due to occasional cancellations or additions (e.g., monthly sampling along Line
498 90.0 in 1998). Among all lines, Line 90.0 recorded the highest number of valid transects
499 (121; Fig. 1b).

500 To further evaluate the quality of observed CHL data, we first interpolated vertical
501 chlorophyll-a profiles from each station onto a standardized 0–200 depth grid. Depths
502 with valid data were marked as 1, and those without data were marked as 0. For each
503 station, depths that contained valid data in at least three cruises were defined as
504 climatologically valid layers. The quality of each profile was then calculated as the
505 percentage of these valid layers that were successfully sampled during a given cruise.
506 Results showed that Lines 80.0, 86.7, 90.0, and 93.3 had consistently high data quality,
507 with Line 90.0 standing out due to both dense sampling and superior quality. Therefore,
508 we selected Line 90.0 for detailed analysis.

509 **Satellite Surface CHL Data**

510 Surface CHL data were derived from the Copernicus-GlobColour multi-sensor merged
511 product (OCEANCOLOUR_GLO_BGC_L4_MY_009_104), integrating observations
512 from SeaWiFS, MODIS, MERIS, OLCI, and VIIRS sensors. It provides daily 4-km

resolution surface CHL from Aug 1997 to present, and has been widely employed both for global and regional CCE applications ^{73, 74}.

Physical and Biogeochemical Model Outputs

To further investigate the dynamic mechanisms underlying this MHWs phenomenon, higher-resolution fields were required. Therefore, we incorporated model outputs from the Copernicus Marine Environment Monitoring Service (CMEMS) to assist our analysis. The physical reanalysis product (hereafter referred to as CMEMS-PHY) utilized here was derived from eddy-resolving GLORYS12V1 system (GLOBAL_MULTIYEAR_PHY_001_030), which provides data-assimilated global ocean fields at a horizontal resolution of 1/12° and 50 vertical levels, spanning from 1993 to two months prior to the present. This product has demonstrated improved fidelity in simulating physical processes in the CCE region ⁵³, and can therefore provide seawater temperature, salinity and ocean currents for this study. The biogeochemical model outputs (CMEMS-BGC) are obtained from the Global Ocean Biogeochemistry Hindcast product (GLOBAL_MULTIYEAR_BGC_001_029), which is based on PISCES model ⁷⁵ and forced by FREE-GLORYS2V4 ocean physical hindcast produced at Mercator-Ocean. Notably, no assimilation was applied to this BGC product. It provides daily chlorophyll-a, nitrate, phosphate, silicate, dissolved oxygen and primary production on a uniform 0.25° horizontal grid with 75 standard levels, over the same temporal extent as physical product. Prior to the analysis, variables from the physical products were interpolated onto the same spatial grid of the biogeochemical products to ensure consistency in data format.

SST Data and MHW Identification

We adopted a widely used approach ¹ to define MHW periods, which is when the Sea Surface Temperature (SST) exceed the 90th percentile of the local climatology for at least 5 days, over the period 1993–2022. The SST data were obtained from The daily Optimum Interpolation Sea Surface Temperature (OISST) analysis product ⁷⁶, with a

spatial resolution of 0.25° and spanning from 1920 to the present. Given that the rate of acclimatization or adaptation to warmer conditions is generally assumed to be lower than the current rate of ocean warming for most ecosystems^{2, 44}, we used the period from 1982 to 2022 as a fixed baseline for constructing the climatology. In the following discussion, a month is labeled as an “MHW month” if more than 50% of the study area (Fig. 1) is under MHW condition and the regional mean intensity exceeds 1°C . Note that the long-term trend of SST from 1982-2022 has been removed before identification based on the recommendation of⁷⁷.

Nutrient Supply and Light Availability

As nitrate is the main nutrient limiting primary production in the CCE⁵², we evaluated impacts of nutrient supply on CHL dynamics by quantifying net nitrate flux transported into the CalCOFI region through five boundaries, including three horizontal boundaries (south, north, west; blue box in Fig. 1a) and two vertical boundaries (bottom: 200 m depth; top: 50 m depth). Nitrate fluxes were estimated as the product of daily nitrate concentration (CMEMS-BGC) and velocity (CMEMS-PHY), integrated over the entire cross-sectional area. Notably, advective fluxes directed into the control volume are positive (i.e., poleward flow at southern boundary, equatorward flow at northern boundary, eastward flow at western boundary, upwelling at bottom boundary and downwelling at top boundary).

Light availability in this study is quantified using Photosynthetically Active Radiation (PAR). Monthly mean surface PAR from 2002 to 2022 was obtained from 4-km MODIS (Terra + Aqua; MCD18A2) PAR product, which applies a multi-temporal surface reflectance algorithm and a look-up table approach to estimate incident PAR⁷⁸. Vertical PAR profiles were computed by the surface MODIS PAR, using the same three-waveband light penetration scheme⁷⁹ as the CMEMS-BGC model⁷⁵, incorporating the effects of phytoplankton biomass and self-shading based on CHL profiles from the CMEMS-BGC output.

Date Availability

CalCOFI in-situ observations used in the study were obtained from <https://calcofi.org/data/oceanographic-data/bottle-database/>. SST data were downloaded from National Centers for Environmental Information (<https://www.ncei.noaa.gov/products/optimum-interpolation-sst>). BGC and PHY model products were derived from Copernicus Marine Data Store (<https://data.marine.copernicus.eu/products>). MODIS surface PAR product was downloaded from <https://oceandata.sci.gsfc.nasa.gov/>.

Code availability

Codes for the main results are available via Zenodo <https://zenodo.org/records/17098687>. Three-waveband light penetration scheme can be found through <https://forge.nemo-ocean.eu/nemo/nemo/-/tree/main/src/OCE/TRA>.

Reference

1. Hobday AJ, *et al.* A hierarchical approach to defining marine heatwaves. *Progress in oceanography* **141**, 227-238 (2016).
2. Oliver EC, *et al.* Marine heatwaves. *Annual review of marine science* **13**, 313-342 (2021).
3. Frölicher TL, Fischer EM, Gruber N. Marine heatwaves under global warming. *Nature* **560**, 360-364 (2018).
4. Oliver EC, *et al.* Longer and more frequent marine heatwaves over the past century. *Nature communications* **9**, 1324 (2018).
5. Eakin CM, Sweatman HP, Brainard RE. The 2014–2017 global-scale coral bleaching event: insights and impacts. *Coral Reefs* **38**, 539-545 (2019).
6. Smith KE, *et al.* Biological impacts of marine heatwaves. *Annual review of marine science* **15**, 119-145 (2023).
7. Wernberg T, *et al.* An extreme climatic event alters marine ecosystem structure in a global biodiversity hotspot. *Nature Climate Change* **3**, 78-82 (2013).
8. Smale DA, *et al.* Marine heatwaves threaten global biodiversity and the provision of ecosystem services. *Nature Climate Change* **9**, 306-312 (2019).
9. Capotondi A, *et al.* A global overview of marine heatwaves in a changing climate. *Communications Earth & Environment* **5**, 701 (2024).
10. Gruber N, Boyd PW, Frölicher TL, Vogt M. Biogeochemical extremes and compound

598 events in the ocean. *Nature* **600**, 395-407 (2021).

599 11. Le Grix N, Burger FA, Frölicher TL. Surface and subsurface compound marine
600 heatwave and biogeochemical extremes under Climate change. *Global Biogeochemical*
601 *Cycles* **39**, e2025GB008514 (2025).

602 12. Hauri C, *et al.* More than marine heatwaves: a new regime of heat, acidity, and low
603 oxygen compound extreme events in the Gulf of Alaska. *AGU Advances* **5**,
604 e2023AV001039 (2024).

605 13. Wong J, Münnich M, Gruber N. Column-compound extremes in the global ocean. *AGU*
606 *Advances* **5**, e2023AV001059 (2024).

607 14. Smith KE, *et al.* Socioeconomic impacts of marine heatwaves: Global issues and
608 opportunities. *Science* **374**, eabj3593 (2021).

609 15. Holbrook NJ, *et al.* A global assessment of marine heatwaves and their drivers. *Nature*
610 *communications* **10**, 2624 (2019).

611 16. Frölicher TL, Laufkötter C. Emerging risks from marine heat waves. *Nature*
612 *communications* **9**, 650 (2018).

613 17. Marañón E. Cell size as a key determinant of phytoplankton metabolism and
614 community structure. *Annual review of marine science* **7**, 241-264 (2015).

615 18. Falkowski PG, Fenchel T, DeLong EF. The microbial engines that drive Earth's
616 biogeochemical cycles. *science* **320**, 1034-1039 (2008).

617 19. Thomas MK, Kremer CT, Klausmeier CA, Litchman E. A global pattern of thermal
618 adaptation in marine phytoplankton. *Science* **338**, 1085-1088 (2012).

619 20. Barton AD, Irwin AJ, Finkel ZV, Stock CA. Anthropogenic climate change drives shift
620 and shuffle in North Atlantic phytoplankton communities. *Proceedings of the National*
621 *Academy of Sciences* **113**, 2964-2969 (2016).

622 21. Fernández-González C, Tarran GA, Schuback N, Woodward EMS, Arístegui J,
623 Marañón E. Phytoplankton responses to changing temperature and nutrient availability
624 are consistent across the tropical and subtropical Atlantic. *Communications Biology* **5**,
625 1035 (2022).

626 22. Le Grix N, Zscheischler J, Laufkötter C, Rousseaux CS, Frölicher TL. Compound high
627 temperature and low chlorophyll extremes in the ocean over the satellite period.
628 *Biogeosciences Discussions* **2020**, 1-26 (2020).

629 23. Noh KM, Lim H-G, Kug J-S. Global chlorophyll responses to marine heatwaves in
630 satellite ocean color. *Environmental Research Letters* **17**, 064034 (2022).

631 24. Zhan W, Zhang Y, He Q, Zhan H. Shifting responses of phytoplankton to atmospheric
632 and oceanic forcing in a prolonged marine heatwave. *Limnology and oceanography* **68**,
633 1821-1834 (2023).

- 634 25. Hayashida H, Matear RJ, Strutton PG. Background nutrient concentration determines
635 phytoplankton bloom response to marine heatwaves. *Global change biology* **26**, 4800-
636 4811 (2020).
- 637 26. Peña MA, Nemcek N, Robert M. Phytoplankton responses to the 2014–2016 warming
638 anomaly in the northeast subarctic Pacific Ocean. *Limnology and Oceanography* **64**,
639 515-525 (2019).
- 640 27. Delgadillo-Hinojosa F, *et al.* Impacts of the 2014–2015 warm-water anomalies on
641 nutrients, chlorophyll-a and hydrographic conditions in the coastal zone of northern
642 Baja California. *Journal of Geophysical Research: Oceans* **125**, e2020JC016473
643 (2020).
- 644 28. Wyatt AM, Resplandy L, Marchetti A. Ecosystem impacts of marine heat waves in the
645 northeast Pacific. *Biogeosciences* **19**, 5689-5705 (2022).
- 646 29. Zhan W, Feng M, Zhang Y, Shen X, Zhan H, He Q. Reduced and smaller phytoplankton
647 during marine heatwaves in eastern boundary upwelling systems. *Communications*
648 *Earth & Environment* **5**, 629 (2024).
- 649 30. Di Lorenzo E, Mantua N. Multi-year persistence of the 2014/15 North Pacific marine
650 heatwave. *Nature Climate Change* **6**, 1042-1047 (2016).
- 651 31. Amaya DJ, Miller AJ, Xie S-P, Kosaka Y. Physical drivers of the summer 2019 North
652 Pacific marine heatwave. *Nature communications* **11**, 1903 (2020).
- 653 32. Wei X, Li KY, Kilpatrick T, Wang M, Xie SP. Large-scale conditions for the record-
654 setting Southern California marine heatwave of August 2018. *Geophysical Research*
655 *Letters* **48**, e2020GL091803 (2021).
- 656 33. Zaba KD, Rudnick DL, Cornuelle BD, Gopalakrishnan G, Mazloff MR. Volume and
657 heat budgets in the coastal California current system: Means, annual cycles, and
658 interannual anomalies of 2014–16. *Journal of Physical Oceanography* **50**, 1435-1453
659 (2020).
- 660 34. Cavole LM, *et al.* Biological impacts of the 2013–2015 warm-water anomaly in the
661 Northeast Pacific: winners, losers, and the future. *Oceanography* **29**, 273-285 (2016).
- 662 35. Closset I, McNair HM, Brzezinski MA, Krause JW, Thamtrakoln K, Jones JL. Diatom
663 response to alterations in upwelling and nutrient dynamics associated with climate
664 forcing in the California Current System. *Limnology and Oceanography* **66**, 1578-1593
665 (2021).
- 666 36. Landry MR, Freibott AL, Stukel MR, Selph KE, Allen AE, Rabines A. Phytoplankton
667 growth and grazing dynamics during anomalous heat wave and suppressed upwelling
668 conditions in the southern California Current. *Deep Sea Research Part I:*
669 *Oceanographic Research Papers* **210**, 104353 (2024).
- 670 37. McCabe RM, *et al.* An unprecedented coastwide toxic algal bloom linked to anomalous

- 671 ocean conditions. *Geophysical research letters* **43**, 10,366-310,376 (2016).
- 672 38. Fischer AD, *et al.* Nutrient limitation dampens the response of a harmful algae to a
673 marine heatwave in an upwelling system. *Limnology and Oceanography*, (2024).
- 674 39. Zhang Y, Du Y, Feng M, Hobday AJ. Vertical structures of marine heatwaves. *Nature*
675 *Communications* **14**, 6483 (2023).
- 676 40. Köhn EE, Vogt M, Münnich M, Gruber N. On the vertical structure and propagation of
677 marine heatwaves in the Eastern Pacific. *Journal of Geophysical Research: Oceans*
678 **129**, e2023JC020063 (2024).
- 679 41. Plume G, *et al.* Vertical structure of subsurface marine heatwaves in a shallow
680 nearshore upwelling system. *Scientific Reports* **15**, 6353 (2025).
- 681 42. Yuan T, Zhang J, Yang S, Su Q, Zhao Z, Ren K. Vertical structures of marine heatwaves
682 in the South China Sea: Characteristics, drivers and impacts on chlorophyll
683 concentration. *Journal of Geophysical Research: Oceans* **129**, e2024JC021091 (2024).
- 684 43. Viljoen JJ, Sun X, Brewin RJ. Climate variability shifts the vertical structure of
685 phytoplankton in the Sargasso Sea. *Nature Climate Change* **14**, 1292-1298 (2024).
- 686 44. Cullen JJ. Subsurface chlorophyll maximum layers: enduring enigma or mystery
687 solved? *Annual Review of Marine Science* **7**, 207-239 (2015).
- 688 45. Ren X, Liu W, Capotondi A, Amaya DJ, Holbrook NJ. The Pacific Decadal Oscillation
689 modulated marine heatwaves in the Northeast Pacific during past decades.
690 *Communications Earth & Environment* **4**, 218 (2023).
- 691 46. Chen TC, Kahru M, Landry MR, Ohman MD, Thompson AR, Stukel MR. Multi-
692 Trophic Level Responses to Marine Heatwave Disturbances in the California Current
693 Ecosystem. *Ecology Letters* **27**, e14502 (2024).
- 694 47. McClatchie S, *et al.* State of the California current 2015-16: comparisons with the
695 1997-98 El Nino. (2016).
- 696 48. Fewings MR, Brown KS. Regional structure in the marine heat wave of summer 2015
697 off the western United States. *Frontiers in Marine Science* **6**, 564 (2019).
- 698 49. Dalsin M, Walter RK, Mazzini PL. Effects of basin-scale climate modes and upwelling
699 on nearshore marine heatwaves and cold spells in the California Current. *Scientific*
700 *reports* **13**, 12389 (2023).
- 701 50. Cervantes BT, Fewings MR, Risien CM. Subsurface temperature anomalies off Central
702 Oregon during 2014–2021. *Journal of Geophysical Research: Oceans* **129**,
703 e2023JC020565 (2024).
- 704 51. Landry MR, Freibott AL, Beatty JL, Selph KE. Phytoplankton biomass responses to a
705 marine heat wave align with altered nitracline depth. *Limnology and Oceanography* **69**,
706 1683-1694 (2024).

- 707 52. Rykaczewski RR, Dunne JP. Enhanced nutrient supply to the California Current
708 Ecosystem with global warming and increased stratification in an earth system model.
709 *Geophysical Research Letters* **37**, (2010).
- 710 53. Amaya DJ, Alexander MA, Scott JD, Jacox MG. An evaluation of high-resolution
711 ocean reanalyses in the California current system. *Progress in Oceanography* **210**,
712 102951 (2023).
- 713 54. Alexander MA, *et al.* A survey of coastal conditions around the continental US using a
714 high-resolution ocean reanalysis. *Progress in Oceanography* **216**, 103055 (2023).
- 715 55. Zaba KD, Rudnick DL. The 2014–2015 warming anomaly in the Southern California
716 Current System observed by underwater gliders. *Geophysical Research Letters* **43**,
717 1241-1248 (2016).
- 718 56. Zheng J, *et al.* Phytoplankton response to the record-breaking marine heatwave in the
719 summer of 2020 in the South China Sea. *Journal of Geophysical Research: Oceans*
720 **129**, e2024JC021275 (2024).
- 721 57. Beckmann A, Hense I. Beneath the surface: Characteristics of oceanic ecosystems
722 under weak mixing conditions—A theoretical investigation. *Progress in Oceanography*
723 **75**, 771-796 (2007).
- 724 58. Kavanaugh MT, Nielsen KJ, Chan FT, Menge BA, Letelier RM, Goodrich LM.
725 Experimental assessment of the effects of shade on an intertidal kelp: do phytoplankton
726 blooms inhibit growth of open coast macroalgae? *Limnology and Oceanography* **54**,
727 276-288 (2009).
- 728 59. Shigesada N, Okubo A. Analysis of the self-shading effect on algal vertical distribution
729 in natural waters. *Journal of Mathematical Biology* **12**, 311-326 (1981).
- 730 60. Moreira-Coello V, Mouriño-Carballido B, Marañón E, Fernández-Carrera A, Bode A,
731 Varela MM. Biological N₂ fixation in the upwelling region off NW Iberia: magnitude,
732 relevance, and players. *Frontiers in Marine Science* **4**, 303 (2017).
- 733 61. Mouriño-Carballido B, *et al.* Magnitude of nitrate turbulent diffusion in contrasting
734 marine environments. *Scientific Reports* **11**, 18804 (2021).
- 735 62. Myers TA, Mechoso CR, Cesana GV, DeFlorio MJ, Waliser DE. Cloud feedback key
736 to marine heatwave off Baja California. *Geophysical Research Letters* **45**, 4345-4352
737 (2018).
- 738 63. Cloern JE. The relative importance of light and nutrient limitation of phytoplankton
739 growth: a simple index of coastal ecosystem sensitivity to nutrient enrichment. *Aquatic*
740 *ecology* **33**, 3-15 (1999).
- 741 64. Shiozaki T, Fujiwara A, Sugie K, Nishino S, Makabe A, Harada N. Bottom-associated
742 phytoplankton bloom and its expansion in the Arctic Ocean. *Global Change Biology*
743 **28**, 7286-7295 (2022).

- 744 65. Hu Q, *et al.* Seasonal variability of phytoplankton biomass revealed by satellite and
745 BGC-Argo data in the central tropical Indian Ocean. *Journal of Geophysical Research:*
746 *Oceans* **127**, e2021JC018227 (2022).
- 747 66. Gomes DG, *et al.* An updated end-to-end ecosystem model of the northern California
748 Current reflecting ecosystem changes due to recent marine heatwaves. *PLoS One* **19**,
749 e0280366 (2024).
- 750 67. Iglesias IS, Fiechter J, Santora JA, Field JC. Vertical distribution of mesopelagic fishes
751 deepens during marine heatwave in the California Current. *ICES Journal of Marine*
752 *Science* **81**, 1837-1849 (2024).
- 753 68. Ohman MD, Barbeau K, Franks PJ, Goericke R, Landry MR, Miller AJ. Ecological
754 transitions in a coastal upwelling ecosystem. *Oceanography* **26**, 210-219 (2013).
- 755 69. Franks PJ, *et al.* Modeling physical-biological responses to climate change in the
756 California Current System. *Oceanography* **26**, 26-33 (2013).
- 757 70. Cordero-Quirós N, Miller AJ, Pan Y, Balitaan L, Curchitser E, Dussin R. Physical-
758 Ecological Response of the California Current System to ENSO events in ROMS-
759 NEMURO. *Ocean Dynamics* **72**, 21-36 (2022).
- 760 71. Cordero-Quirós N, Miller AJ, Subramanian AC, Luo JY, Capotondi A. Composite
761 physical–biological El Niño and La Niña conditions in the California Current System
762 in CESM1-POP2-BEC. *Ocean Modelling* **142**, 101439 (2019).
- 763 72. Miller AJ, Song H, Subramanian AC. The physical oceanographic environment during
764 the CCE-LTER Years: Changes in climate and concepts. *Deep Sea Research Part II:*
765 *Topical Studies in Oceanography* **112**, 6-17 (2015).
- 766 73. Mélin F, Vantrepotte V, Chuprin A, Grant M, Jackson T, Sathyendranath S. Global
767 trends in chlorophyll concentration observed with the satellite ocean colour data record.
768 In: *Living Planet Symposium*) (2016).
- 769 74. Stone HB, Banas NS, MacCready P, Kudela RM, Ovall B. Linking chlorophyll
770 concentration and wind patterns using satellite data in the central and northern
771 california current system. *Frontiers in Marine Science* **7**, 551562 (2020).
- 772 75. Aumont O, Éthé C, Tagliabue A, Bopp L, Gehlen M. PISCES-v2: an ocean
773 biogeochemical model for carbon and ecosystem studies. *Geoscientific Model*
774 *Development Discussions* **8**, 1375-1509 (2015).
- 775 76. Reynolds RW, Smith TM, Liu C, Chelton DB, Casey KS, Schlax MG. Daily high-
776 resolution-blended analyses for sea surface temperature. *Journal of climate* **20**, 5473-
777 5496 (2007).
- 778 77. Smith KE, *et al.* Baseline matters: Challenges and implications of different marine
779 heatwave baselines. *Progress in Oceanography* **231**, 103404 (2025).
- 780 78. Liang S, Wang D. Moderate resolution imaging spectroradiometer (MODIS)

downward shortwave radiation (MCD18A1) and photosynthetically active radiation (MCD18A2) algorithm theoretical basis document. In: *Google Scholar There is no Corresponding Record for This Reference* (2017).

79. Lengaigne M, *et al.* Influence of the oceanic biology on the tropical Pacific climate in a coupled general circulation model. *Climate Dynamics* **28**, 503-516 (2007).

Acknowledgments

We thank our numerous colleagues and the shipboard operations crews in the CalCOFI and CCE LTER Programs whose decades of work made this study possible. This research was supported by National Science Foundation grant OCE-2224726 to the CCE LTER Program, National Key R&D Program of China (Grant No. 2022YFC3103402), Scientific and technological projects of Zhoushan (2022C01004) and National Natural Science Foundation of China (No. 42576028). We thank the three anonymous referees for their very constructive comments.

Author contributions

J.L. and A.M. designed the study. J.L. conducted the analyses and wrote the first draft of the manuscript under A.M. and P.B.'s instruction. D.A. and Q.W. were involved in improving the manuscript. Y.G. and P.L. contributed to the discussion and revision of the study.

Competing interests

The authors declare no competing interests.

Table. 1 Net nitrate flux anomalies. Net nitrate flux anomalies (unit: kmol/s) at five boundaries and their p-values (T-test), directions into the CCE region are positive.

Boundary	South	North	West	Bottom	Top
Net Nitrate Flux Anomalies	1.81	-0.83	1.90	-1.02	0.38
P-value	0.11	0.40	< 0.01	< 0.01	< 0.01

Fig. 1 MHWs in the CCE and data records of the CalCOFI. (a) Mean MHW intensity based on OISST from 1993 to 2022. Black dots and dashes represent the sampling stations and transect lines of CalCOFI cruises. Green dashes represent the mean surface CHL concentration from Copernicus-GlobColour (1997–2022). Blue box denotes the boundary of the CalCOFI region. (b) Sampling records and its data quality (proportion of valid data) of six CalCOFI Lines from 1993 to 2022.

Fig. 2 MHWs occurrences and PDO index. (a) MHW occurrences in the CalCOFI region based on OISST. Color and radius of unfilled circles represent the monthly mean intensity and spatial coverage (%) of MHWs, respectively. Filled circles indicate months when more than 50% area (Fig. 1) is under MHW conditions and the regional mean intensity exceeds 1 °C, labeled as “MHW month”. Asterisks denote MHW months when CalCOFI cruises were conducted. (b) Pacific Decadal Oscillation (PDO) Index.

Fig. 3 Vertical responses of CHL to MHWs. (a) Scatter density plot of CHL anomalies during MHWs, derived from vertical profiles at all stations across six CalCOFI lines. (b) Boxplot of CHL anomalies at 10-m depth intervals. The vertical dashed line indicates zero anomaly, and red lines denote the median. Green boxes indicate depths where anomalies are statistically different from zero (T-test; $p < 0.05$). Vertically integrated CHL anomalies were calculated separately for the surface layer (from surface to SCML depth) and the subsurface layer (SCML depth to 200-m) at each station, and then averaged across all stations within the CalCOFI region.

Fig. 4 Seasonal patterns of vertical CHL and temperature anomalies. Seasonal anomalies of temperature (a-d) and CHL (e-h) during MHWs along CalCOFI Line 90.0 (DJF, MAM, JJA, SON represent winter: December–February, spring: March–May, summer: June–August, and fall: September–November, respectively). Black and red dashed lines denote mixed layer and subsurface chlorophyll maximum layer (SCML) depth, respectively. Anomalies were calculated based on data from MHW months during which CalCOFI cruises were conducted (asterisks in Fig. 2).

Fig. 5 Composite anomalies of environmental variables during MHWs. (a-f) Composite anomalies of temperature (TEMP; °C), salinity (SALT; PSU), dissolved oxygen (O₂; ml L⁻¹),

CHL ($\mu\text{g L}^{-1}$), phosphate (PO_4 ; $\mu\text{mol L}^{-1}$) and nitrate (NO_3 ; $\mu\text{mol L}^{-1}$) during MHWs, with contours representing climatological values. (g) Vertical profiles of CHL (green), SCML (dark green) and nitrate concentration (blue) under climatology (solid lines) and MHWs (dash lines) states, averaged along offshore distance of CalCOFI Line 90.0.

Fig. 6 Physical conditions during MHWs. Climatological (a-c) profiles of temperature, salinity and cross section velocity and their composite anomalies (d-f) during MHWs along CalCOFI Line 90.0. Black dots denote the anomalies are significantly different from zero (T-test; $p < 0.05$). Arrows in (c) and (f) represent the mean along-section and vertical velocities and their anomalies (only shown when anomalies in both directions are significantly different from zero), vertical component of velocity is multiplied by 1000 for better visualization. Note that the composite anomalies are calculated by the same MHW month as Fig. 5.

Fig. 7 Temporal evolutions of local biogeochemical environments and nitrate flux. (a-c) Vertical anomalies of simulated CHL, dissolved oxygen and nitrate, averaged over the CalCOFI region, shown as a function of time. Dashed and solid lines in (a) refer the climatological and real SCML depth, respectively. (d) Modeled vertical CHL distribution from 2014 to 2015. Dashed and solid contours (white lines) represent the climatological and real $0.4 \mu\text{g L}^{-1}$ CHL isoline (SCML), respectively. PAR at surface is divided by 5 for visualization. (e) Nitrate flux anomalies across the five boundaries of the CalCOFI region: alongshore (blue), cross-shore (green), and vertical (red), with positive values indicating inward transport. Blue and red bars denote anomalies of PAR at the surface and 50-m depth, respectively. (f) Nitrate flux anomalies across bottom and top boundaries.

Fig. 8 Light availability during MHWs. (a) Timeseries of vertical light conditions. Red bars represent the monthly coverage of the MHW area (%). Shading denotes the PAR anomalies at different depth. (b) Black (red) dots represent the monthly PAR at surface and at 50-m depth under normal (MHW) condition. Green and red line refer normalized anomalies of CHL and PAR under MHWs. All values here are regionally averaged over the CalCOFI region.